Journal of Applied Fluid Mechanics, Vol. 18, No. 2, pp. 419-437, 2025.
Available online at www.jafmonline.net, ISSN 1735-3572, EISSN 1735-3645.
https://doi.org/10.47176/jafm.18.2.2813

Numerical Investigation on the Cavitating Flow and the Cavitation-induced Noise in the Pump-jet Propeller

P. Zhang[1], J. Yuan[1], Y. Fu[2†], X. Hou[1] and J. Hao[1]

[1] *National Research Center of Pump, Jiangsu University, Zhenjiang 212013, Jiangsu, China*
[2] *School of Energy and Power Engineering, Jiangsu University, Zhenjiang 212013, Jiangsu, China*

†*Corresponding Author Email: yanxiafu@ujs.edu.cn*

ABSTRACT

The noise hazard posed by cavitation in pump-jet propellers is a significant concern during oceanic operations. This study evaluates the cavitation performance and associated noise characteristics of pump-jet propellers in underwater conditions, further examining the interplay between cavitation phenomena and noise radiation. Cavitation performance across varying advance coefficients was scrutinized using the *k-ω* SST turbulence model alongside the Zwart cavitation model. Employing Lighthill's analogy method and bubble radiation theory, analyses of flow-induced noise and noise due to cavitation were conducted. The findings indicate an intensification of cavitation within the pump-jet with increased rotational speed and a reduction in cavitation number, aligning pressure and velocity distributions with observed cavitation patterns. Cavitation markedly elevates flow-induced noise levels, with noise under cavitation conditions found to be around 50 dB higher compared to non-cavitation conditions. Considering cavitation bubble radiation noise, the volumetric pulsations and their amplitudes in the pump-jet enlarge as the bubbles progress through initial growth to maturity. Predominantly, the noise levels from bubble volume pulsations occur within low to medium frequency ranges.

Article History

Received April 27, 2024
Revised June 30, 2024
Accepted August 29, 2024
Available online December 4, 2024

Keywords:

Pump-jet propeller
Numerical simulation
Acoustic computing
Cavitation
Noise

1. INTRODUCTION

The advancement of various underwater vehicles, such as submarines, torpedoes, and unmanned detectors, has driven the need for improved propeller performance, encompassing noise reduction, efficiency, and cavitation management. Pump-jet propellers, known for their complex architecture and high production costs, are predominantly utilized in military applications. Since the 1980s, pump-jet propeller technology has progressively garnered global research interest (Furuya & Chiang, 1988). These propellers are noted for their excellent stealth capabilities, superior propulsion efficiency, and strong cavitation resistance, making them integral to the propulsion systems of diverse marine equipment (Li et al., 2022). Consequently, the development of efficient, stable, and quiet pump-jet propellers has emerged as a research focus worldwide (Kowalczyk & Felicjancik, 2016).

Under overload conditions, the high-speed rotating rotor blades create a substantial negative pressure zone on the suction side, predisposing the system to cavitation, which significantly degrades the hydrodynamic and acoustic performance of pump-jet propellers (Zhou et al., 2022). Consequently, extensive research on the cavitation characteristics has been undertaken through experimental and numerical simulation approaches (Satyanarayana et al., 2010; Al-Obaidi, 2018; Sun et al., 2022; Avanzi et al., 2023; Gan et al., 2023b; Han et al., 2023; Xu & Lai, 2023). Studies have investigated various phenomena such as tip clearance vortices, bubble distribution on rotor blade surfaces, and the interaction dynamics between cavitation and wakes (Han et al., 2020; Yuan et al., 2020; Zhao et al., 2022). Specifically, Yuan et al. (2020) employed the Detached Eddy Simulation (DES) and Zwart-Gerber-Belamri (ZGB) cavitation model to numerically simulate cavitation in pump-jets, analyzing the evolution of tip clearance vortices and cavitation under diverse operational conditions. Furthermore, Zhao et al. (2022) performed numerical simulations to investigate the hydrodynamic load and wake evolution in a forward-stator pump-jet propeller using DES, analyzing bubble distribution on rotor blade surfaces, blade tip cavitation, and tip clearance cavitation while exploring the interaction mechanisms between cavitation and wakes. Additional research has examined variables such as blade number, tip clearances, and skewed flow angles, which are critical to the hydrodynamic and cavitation performance of pump-jets

Nomenclature

ρ	density	t	time
t	time	C_{vap}	empirical coefficient for the evaporation term
k	turbulent kinetic energy	C_{cond}	empirical coefficient for the condensation term
u_i	velocity component	c_0	speed of sound
u_j		c	speed of sound in water
x_i	coordinate	T_{ij}	Lighthill stress tensor
x_j		τ_{ij}	viscous stress term
G_k	turbulent diffusion term	Q	volume velocity
Γ_k		ρ_0	density of the fluid in the absence of
Y_k		δ_{ij}	Kronecker delta
S_k		q	volume velocity
β^*	user-defined coefficient	r	distance from the center of the sphere
F_{DES}	des model correction factor	V_c	total volume of bubble
C_{DES}		V_i	volume size of each control volume
ω	vorticity	W_A	sound power
L_t	turbulent length scale	M_t	Mach number
Δ_{max}	maximum grid spacing	L_W	sound power level
α_l	volume fraction of liquid	W_{ref}	reference sound power
α_v	volume fraction of vapor	J	advance coefficient
α_{nuc}	volume fraction of vapor core	K_T	thrust coefficient
α_i	volume fraction of the bubble	K_Q	torque coefficient
ρ_l	density of liquid	η	efficiency
ρ_v	density of vapor	v	inflow velocity
m^+	mass transfer rate	D	average diameter of the rotor
m^-		T	thrust
R_B	bubble radius	Q	torque
p	pressure	σ	cavitation number
p_v	saturated vapor pressure	p_{out}	outlet pressure of the external flow field
P_0	far-field pressure	p_v	saturated vapor pressure of water at 25°C

(Qiu et al., 2020; Li et al., 2023a; Gan et al., 2023a). For instance, Li et al. (2023a) analyzed the impact of blade count on the hydrodynamic and cavitation performance of stators and rotors. Qiu et al. (2020) assessed the influence of tip clearances and skewed flow angles on pump-jet performance, finding that skewed flow angles significantly affect efficiency. Gan et al. (2023a) explored how tip clearances impact the cavitation resistance and structural integrity of high-speed pump-jet propellers, concluding that larger tip clearances enhance cavitation resistance but may negatively affect the structural integrity of the pump-jets. Despite extensive research on the cavitation characteristics of pump-jet propellers, literature on predicting cavitation-induced noise remains limited.

Propeller noise constitutes the primary source of acoustic disturbances for underwater vehicles. Investigating the noise performance prediction of pump-jet propellers and developing methods to attenuate this noise are crucial for enhancing the stealth capabilities of these vehicles. In this context, numerous scholars have employed both experimental and numerical simulations to explore this issue (Si et al., 2020; Al-Obaidi, 2023, 2024; Gangipamula et al., 2023; Si et al., 2023). Extensive studies have been conducted, and several strategies have been suggested to mitigate the noise from pump-jet propellers. Shi et al. (2022) elucidated the vibration and acoustic radiation characteristics of underwater pump-jet propellers through a combination of experiments and numerical simulations. Their findings demonstrate that numerical simulation techniques, incorporating computational fluid dynamics, coupled finite element analysis, and boundary element methods, can accurately forecast the vibration and acoustic radiation behaviors of pump-jet propellers. Huang et al. (2022) introduced a device to eliminate tip clearances in pump-jets, which reduced the pulsating pressure frequency and amplitude on the blades, substantially lowering acoustic power output. Qin et al. (2019) utilized a serrated duct to diminish the noise levels of pump-jets, with noise assessments based on DES and FW-H equations, showing a maximum efficiency loss of 2% and a noise reduction of up to 4.88 dB compared to conventional ducts. Su et al. (2021) derived blade excitation forces via CFD simulations and forecasted the acoustic-vibration response of pump-jets using a coupled finite element/boundary element model. Analyses were performed on the impact of excitation forces on modal vibrations, acoustic power radiation, and radiation directivity. Li et al. (2023b) discovered that stator pre-swirl angles significantly influence the hydrodynamic and noise performance of pump-jet propellers, noting that turbulence amplitude escalates with increased pre-swirl angles, with the lowest noise levels observed at the minimal pre-swirl angle. Shi et al. (2022) examined the noise characteristics of a submarine equipped with pump-jet propellers, analyzing

both flow noise and structural noise concurrently. Zhang et al. (2024) identified that the clocking effect of pre-swirl stators considerably affects rotor excitation forces, vibration, and acoustic radiation in pump-jets. Currently, there is limited research on cavitation noise of pump-jet propulsors, with minimal consideration given to the influence of bubble cavitation noise.

This study aims to enhance the propulsion performance and stealth capabilities of underwater vehicles by focusing on internal flow stability, fluid dynamic performance, and noise characteristics of pump-jet propellers under cavitation conditions during underwater operation. The findings are expected to contribute to the design optimization of pump-jets and overall performance enhancement of underwater vehicles.

2. MATHEMATICAL MODEL

2.1 Turbulence Model

In steady-state simulations, the SST *k-ω* turbulence model (Menter, 1994) was employed, combining the robustness of the *k-ω* model in the near-wall region with the *k-ε* model's efficacy in resolving free turbulence in the far field. This model is particularly accurate in predicting adverse pressure gradients and separated flows, due to its wide applicability, direct usability, and high precision.

For unsteady simulations of pump-jet propellers, the Detached Eddy Simulation (DES) model based on SST *k-ω* (Spalart, 1997) was utilized. DES integrates the computational techniques of RANS and LES, employing RANS to resolve small-scale turbulence near the wall and LES for large-scale turbulence in separated regions away from the wall. This method offers an approximation of LES-level accuracy with enhanced computational efficiency.

The DES model facilitates the transition from the RANS approach to the LES method by modifying the turbulence dissipation term in the *k*-equation, which governs the transport of turbulent kinetic energy:

$$\frac{\partial}{\partial t}(\rho k)+\frac{\partial}{\partial x_i}(\rho k u_i)=\frac{\partial}{\partial x_j}\left(\Gamma_k \frac{\partial k}{\partial x_j}\right)+G_k-Y_k+S_k \tag{1}$$

where t represents time, ρ represents fluid density, k represents turbulent kinetic energy, u_i represents the velocity component in the i direction, x_i and x_j represent coordinate components, G_k represents the production of turbulent kinetic energy due to mean velocity gradients, Γ_k represents the effective diffusivity of turbulent kinetic energy k, Y_k represents the diffusion caused by turbulence, and S_k is a user-defined source term.

The definition of Y_k is given by:

$$Y_k=\rho\beta^* F_{DES} k\omega \tag{2}$$

where β^* is a user-defined coefficient, F_{DES} is a correction factor for the DES model, and ω represents the vorticity.

The correction factor F_{DES} is defined as:

$$F_{DES}=\max\left(\frac{L_t}{C_{DES}\Delta_{\max}},1\right) \tag{3}$$

where L_t is the turbulent length scale, C_{DES} is a constant specific to the DES model, and $\Delta_{\max}$ is the maximum grid spacing.

2.2 Cavitation Model

The ZGB model, an advanced cavitation model based on the Rayleigh-Plesset equation, effectively simulates the intricacies of cavitation flow and is extensively employed in numerical simulations of such phenomena. Consequently, the ZGB cavitation model (Zwart et al., 2004) was utilized in the numerical simulation of cavitation flow within pump-jet propulsion systems. The model is formulated as follows:

$$\frac{\partial}{\partial t}(\alpha_l\rho_l)+\nabla(\alpha_l\rho_l u_j)=m^+-m^- \tag{4}$$

$$m^+=C_{vap}\frac{3\alpha_{nuc}(1-\alpha_v)\rho_v}{R_B}\sqrt{\frac{2}{3}\frac{(p-p_v)}{\rho_l}} \tag{5}$$

$$m^-=C_{cond}\frac{3\alpha_v\rho_v}{R_B}\sqrt{\frac{2}{3}\frac{(p-p_v)}{\rho_l}} \tag{6}$$

where α_l and α_v represent the volume fractions of liquid and vapor, respectively, ρ_l and ρ_v are the densities of liquid and vapor, α_{nuc} represents the vapor core volume fraction, u_j is the velocity component in the j direction, m^+ and m^- are the mass transfer rates due to evaporation and condensation, respectively, R_B represents the bubble radius, and is set to $1\times10^6\,m$, p is the pressure in the flow field, p_v is the saturated vapor pressure, and is set to 3540 Pa. C_{vap} is the empirical coefficient for the evaporation term, with a value of C_{vap}=50. C_{cond} is the empirical coefficient for the condensation term, with a value of C_{cond}=0.01.

The cavitation number (σ) of the pump-jet propeller was calculated using the following equation:

$$\sigma=\frac{p_{out}-p_v}{0.5\rho u^2} \tag{7}$$

Where p_{out} is the outlet pressure of the external flow field, Pa; p_v is the saturated vapor pressure of water at 25°C, Pa; u is the average inflow velocity, m/s.

2.3 Lighthill's Analogy Method

In scenarios where volume pulsation radiation noise is not considered, this study employs Lighthill's Analogy method (Lighthill, 1952; Hashem et al., 2017) for calculations. The method is formulated using the following expressions:

$$\frac{\partial^2(\rho-\rho_0)}{\partial t^2}-c_0^2\frac{\partial^2}{\partial x_i\partial x_j}(\rho-\rho_0)=\frac{\partial^2 T_{ij}}{\partial x_i x_j} \tag{8}$$

$$T_{ij}=\rho u_i u_j-\tau_{ij}+\delta_{ij}\left[(p-p_0)-c_0^2(\rho-\rho_0)\right] \tag{9}$$

where ρ is the fluid density, ρ_0 is the density of the fluid in the absence of disturbances, c_0 is the speed of sound, T_{ij} represents the Lighthill stress tensor, u_i and u_j represent velocity components in the *i* and *j* directions, respectively. τ_{ij} is the viscous stress term, *p* is the pressure experienced by the fluid, and p_0 is the pressure experienced by the fluid in the absence of disturbances.

2.4 Spherical Bubble Radiation Theory

Bubble noise primarily arises from the volume pulsation of the bubble and the monopole noise generated during bubble collapse. The issue of bubble radiation noise in the flow field can be addressed through the theory of spherical bubble radiation. Utilizing the continuity condition of the bubble wall velocity, the acoustic pressure associated with bubble volume pulsation radiation noise can be linked to the bubble motion parameters (Lighthill, 1952; Ghasemian & Nejat, 2015; Mohamed, 2016). Considering the bubble as a simple pulsating sound source, the acoustic pressure at a monitoring point located a distance r from the center of the sphere can be described as follows:

$$p(r,t)=\frac{\rho_0}{4\pi r}\frac{\partial}{\partial t}Q\left(t-\frac{r}{c_0}\right) \tag{10}$$

where *Q* represents the volume velocity and *r* represents the distance from the center of the sphere.

For a uniformly pulsating spherical bubble, the volume velocity is expressed as:

$$Q(t)=4\pi R^2(t)\dot{R}(t) \tag{11}$$

The volume pulsation of the bubble is related to its volume, so it is necessary to collect the time-varying volume data of the bubble first. The formula for calculating the size of the bubble volume is:

$$V_c=\sum_{i=1}^{N}\alpha_i V_i \tag{12}$$

where V_c is the total volume of the bubble in m^3; *N* is the total number of control volumes; α_i is the volume fraction of the bubble in each control volume; V_i represents the volume size of each control volume in m^3.

Once the center of the pulsating spherical sound source has been identified, the acoustic pressure resulting from the pulsation of the bubble volume can be calculated at any acoustic monitoring point using Equation (12).

2.5 Calculation Method for Sound Power Level Distribution in Cavitation Flow Field

Sound power represents the total energy that a sound source radiates into a specific space per unit of time, and it is quantified in watts (W). The equation for calculating sound power is presented as follows (Proudman, 1952; Chang et al., 2018):

$$W_A=\alpha\rho_{L_t}\varepsilon M_t^5 \tag{13}$$

$$M_t=\frac{\sqrt{2k}}{c} \tag{14}$$

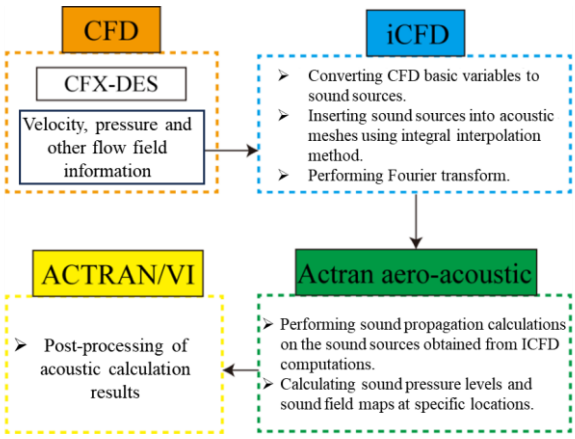

Fig. 1 Flow chart for flow induced noise calculation

where α is a constant typically set to α=0.1, and *c* represents the speed of sound in water, with a value of *c*=1500 m/s.

The expression for sound power level is given by:

$$L_W=10\lg\frac{W_A}{W_{ref}} \tag{15}$$

In this equation, W_{ref} represents the reference sound power, with a value of $W_{ref}=10^{-12}$W/m^3.

Figure 1 delineates the principal technical process for calculating flow-induced noise. Flow field data derived from CFD simulations serve as the input for noise calculations. Velocity, pressure, and density data from these simulations are imported into Actran for noise analysis. Within Actran iCFD, the unsteady flow field solutions are used to interpolate and integrate these flow field variables into the acoustic mesh through integral interpolation. Subsequently, a Fourier transform is applied to convert the data into the time-frequency domain. The Actran Aero-Acoustic solver then computes the sound radiation based on the sources determined by iCFD computations.

3. Calculation Model

3.1 Calculation Model

A pump-jet propeller equipped with a trailing stator was analyzed. Figure 2 presents a schematic of the 3D geometric model of the pump-jet propeller, which includes 7 rotor blades and 9 stator blades. The duct's cross-sectional shape adopts a NACA66 airfoil profile. Detailed geometric parameters are outlined in Table 1. To streamline the calculation model and promote uniform flow, an elliptical diffuser cap is positioned at the front end of the pump-jet propeller's hub, and a wake cap is affixed at the rear end.

Figure 3 illustrates the schematic of the computational domain used for the numerical simulation of the pump-jet propeller. The domain is segmented into the external flow field, rotor domain, and stator domain. The external flow field is modeled by encasing the pump-jet propeller within

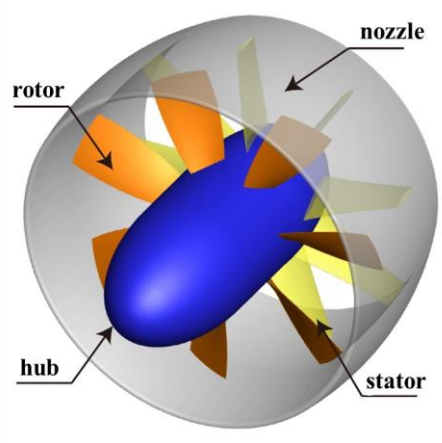

Fig. 2 The 3D model of pump-jet propeller

Table 1 Geometric parameters of the model pump-jet. Propeller

parameter	value
blade number of rotor	7
blade number of stator	9
pipe airfoil profile	NACA66
Maximum rotor diameter	349.2
Rotor tip clearance(mm)	1

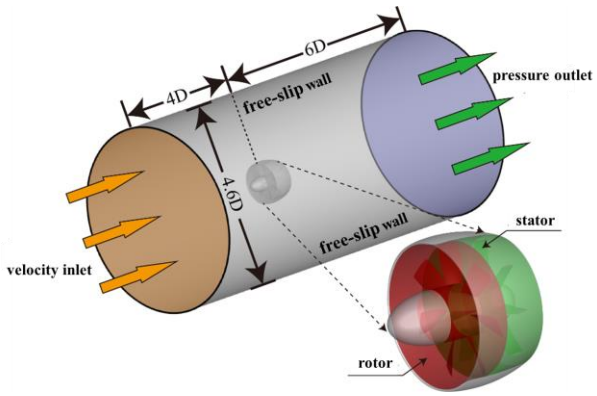

Fig. 3 Calculation domain division and boundary conditions of the model pump-jet propeller

a coaxial cylinder, which has a diameter 4.6 times that of the rotor (D) and a length 10 times the rotor diameter (D).

3.2 Mesh Generation and Grid Independence Check

Figure 4 depicts the mesh generation for both the fluid domains and the acoustic calculation domains. As illustrated in Fig. 3(a), the fluid domains utilize a grid configuration. Considering the complex blade structure and significant distortion at the rotor blades of the pump-jet propeller, hexahedral structured mesh generation is employed within the computational domains using ANSYS ICEM software. To enhance the capture of detailed flow characteristics within the pump-jet propeller and its wake region, local refinement is applied around the blades and wake area, maintaining a grid quality index above 0.4. For the near-wall grid, the average y+ value for various components is approximately 4.5. The global grid

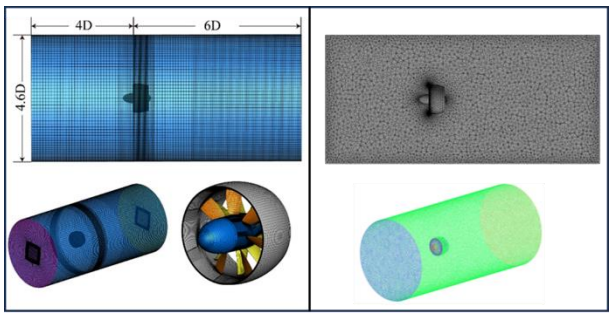

(a) (b)

Fig. 4 Distribution of grids for fluid and acoustic computational domains of the pump-jet propeller:(a) global grid for CFD computational domain;(b) global grid for acoustic computational domain

for the acoustic computational domains aligns structurally with the fluid domains. An unstructured grid strategy is adopted, and Fig. 3(b) demonstrates the internal grid distribution within the computational domain, featuring local refinement adjacent to the pump-jet propeller.

To ascertain that the grid count does not influence the outcomes of the numerical simulations, four different grid configurations were employed to conduct simulations under the design condition (advance coefficient J=0.948). Grid independence is confirmed by evaluating the open water performance of the pump-jet propeller.

The performance parameters of a pump-jet propeller operating in open water are typically characterized by non-dimensional coefficients such as the advance coefficient (J), thrust coefficient (K_T), torque coefficient (K_Q), and efficiency (η). These coefficients can be calculated using the formulas provided below:

$$J = \frac{v}{nD} \tag{16}$$

$$K_T = \frac{T}{\rho n^2 D^4} \tag{17}$$

$$K_Q = \frac{Q}{\rho n^2 D^5} \tag{18}$$

$$\eta = \frac{JK_T}{2\pi K_Q} \tag{19}$$

where v represents the inflow velocity, n is the rotational speed of the rotor, D denotes the average diameter of the rotor, ρ is the water density, T represents the thrust of the entire pump-jet propeller system, and Q represents the torque of the rotor.

Data from Table 2 and Fig 5 indicate that the deviations in K_T, K_Q, and η across varying grid numbers are minor, all remaining below 2%. When the grid count exceeded 1.118 million, the open water performance of the pump-jet propeller stabilized. Therefore, to balance computational accuracy and efficiency, the third grid configuration was chosen for the numerical simulations.

Table 2 Different sets of grids and distribution

Mesh	Rotor	Stator	Other region	Total
Mesh1	396	180	149	726
Mesh2	529	232	197	959
Mesh3	610	278	229	1118
Mesh4	943	429	355	1728

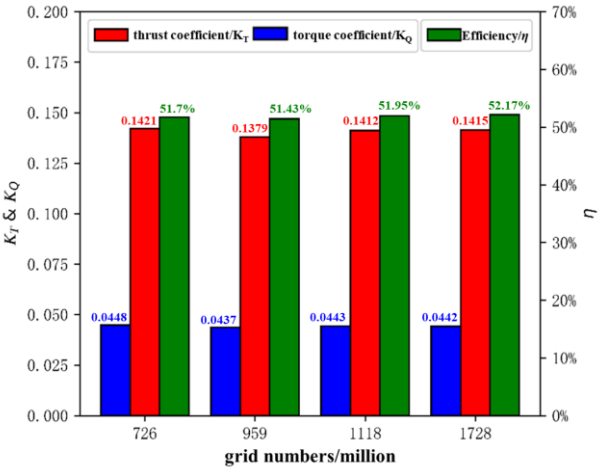

Fig. 5 Mesh independence analysis of pump-jet propeller calculation model

3.3 Calculation Settings

The numerical simulations were conducted using ANSYS CFX software. At the inlet of the external flow field, a velocity inlet boundary condition was established with a velocity magnitude of v=7m/s and a turbulence intensity of I=5%. The outlet was configured as a pressure outlet with a relative pressure of 0 Pa. Moreover, the wall of the external flow field was defined as a free-slip boundary, whereas all other walls were set as no-slip boundaries. The pump-jet propeller is positioned 4D from the inlet. Interfaces were established at the inlets and outlets of the three computational domains. For steady-state simulations, the interaction between the rotor and stator was set in frozen rotor mode. In transient simulations, this interaction was defined as transient rotor-stator mode.

To expedite convergence in transient calculations, results from steady-state numerical simulations were utilized as initial conditions for the transient cavitation simulations. The time step (Δt) for the unsteady cavitation flow calculations was set to 1.33×10^{-4}s, with a total simulation time of 0.48 s.

3.4 Acoustic Calculation Settings

The flow field information from unsteady simulations was incorporated into the acoustic calculation grid to predict the noise generated by the pump-jet propeller. The numerical simulation results were analyzed in Actran, where noise sources were extracted, and water was selected as the acoustic propagation medium. The acoustic analysis can encompass a frequency range from 0 to 2000 Hz. The boundary conditions for the acoustic model were simplified by designating the outer surface of the cylindrical domain as a free sound transmission boundary, while the outer wall surfaces of the duct and the diffuser cap were defined as rigid boundaries, thus ignoring the transmission of flow field noise on the pump-jet's outer wall. The stator domain was modeled as a volume sound source, and the rotor-stator interface components were established as the Lighthill surface, which facilitates the extraction of noise data from the rotor's rotating domain via the sound source surface. The external flow field of the pump-jet was designated as the acoustic propagation domain, where the volume sound source and the acoustic propagation domain together form the finite element domain.

Table 3 Geometric parameters of propeller E779A

parameter	symbol	unit	value
diameter	D	[m]	0.227
blade number	Z	[-]	4
pitch ratio	P/D	[-]	1.2
inclination angle at blade tip	θ_s^{tip}	[°]	4.8
longitudinal inclination angle	i	[°]	4.6

4. EXPERIMENTAL VALIDATION

Due to the challenges of conducting experiments in this study and the absence of experimental data, the E779A propeller was selected for validation of the numerical simulation methods presented herein. The E779A, a four-bladed propeller, has publicly available experimental models and hydrodynamic performance data documented in the literature (Vaz et al., 2015). Employing the CFD method described earlier, both the hydrodynamic and cavitation performance of the E779A propeller were evaluated against the corresponding experimental data. The geometric parameters of the E779A propeller are detailed in Table 3. Figure 6 depicts the computational domain for the E779A propeller, with hydrodynamic performance assessments conducted using velocity inlet and pressure outlet boundary conditions.

Figure 7 presents a comparison between the hydrodynamic performance of the E779A propeller and experimental results across various advance coefficients.

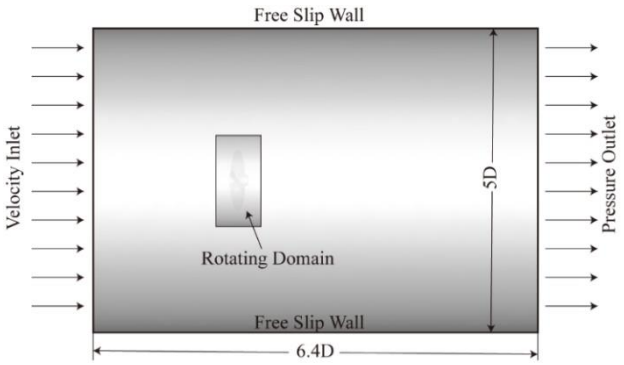

Fig. 6 Schematic diagram of calculation domain for propeller E779A

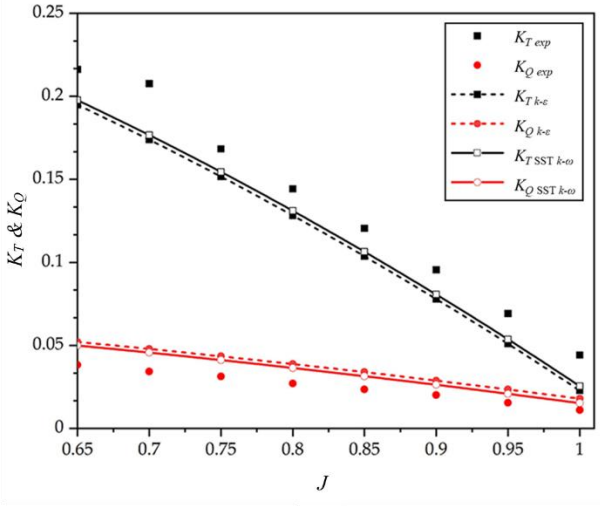

Fig. 7 Comparison of numerical simulation method and experimental open water performance of propeller E779A

The absolute deviations between the computed values and the experimental data for both the thrust coefficient and torque coefficient are within 0.02. These deviations arise due to differences between the experimental setups and the simulated external fluid domains, particularly notable at smaller advance coefficients (J). Despite these discrepancies, the performance curves derived using the SST k-ω turbulence model demonstrate good agreement with the experimental results.

Figure 8 presents a comparison of cavitation distribution between numerical simulations and visualization experiments at an advance coefficient (J) of 0.71 and a cavitation number (σ_n) of 1.763. The contour plot of vapor volume fraction distribution on the rotor blade surface shows that cavitation predominantly occurs on the suction side near the blade tip and leading edge. This pattern closely aligns with the cavitation locations observed in the experiments, indirectly validating the accuracy of the simulation methodology employed in this study.

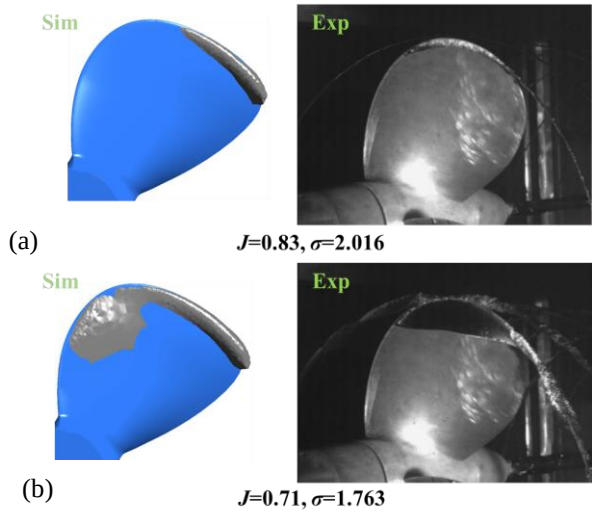

Fig. 8 Experimental verification of cavitation of propeller E779A

5. RESULTS ANALYSIS AND DISCUSSION

5.1 Hydrodynamic Performance Study under Cavitation and Non-cavitation Conditions

As depicted in Fig 9, a comparative analysis of the hydrodynamic efficiency of the pump-jet propeller operating with and without cavitation at different rotational speeds is presented. With increasing speeds, the disparity in efficiency between cavitating and non-cavitating conditions becomes more pronounced. At low speeds, no cavitation occurs, and the efficiency remains consistent. However, as the rotational speed increases, cavitation initiates. At 1250 rpm, the efficiency under cavitation conditions peaks before declining sharply. In contrast, under non-cavitation conditions, the efficiency maximizes at 1450 rpm and shows minimal fluctuation thereafter. Generally, higher speeds increase the susceptibility of the pump-jet propeller to cavitation, and the progression of cavitation significantly influences its hydrodynamic efficiency.

Furthermore, the hydrodynamic performance of the pump-jet propeller was evaluated across a range of cavitation coefficients. Figure 10 illustrates the

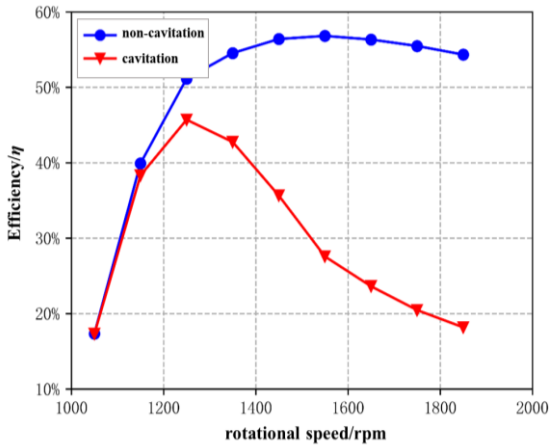

Fig. 9 Comparison of hydrodynamic efficiency of pump-jet propeller before and after cavitation at different rotor rotational speeds

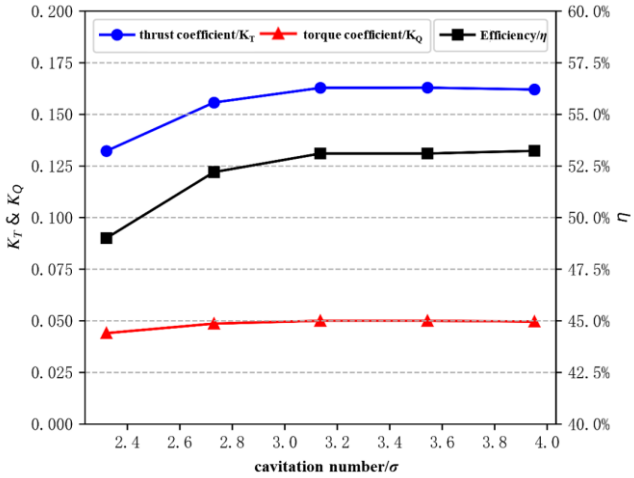

Fig. 10 Hydrodynamic performance of pump-jet propeller under different cavitation numbers

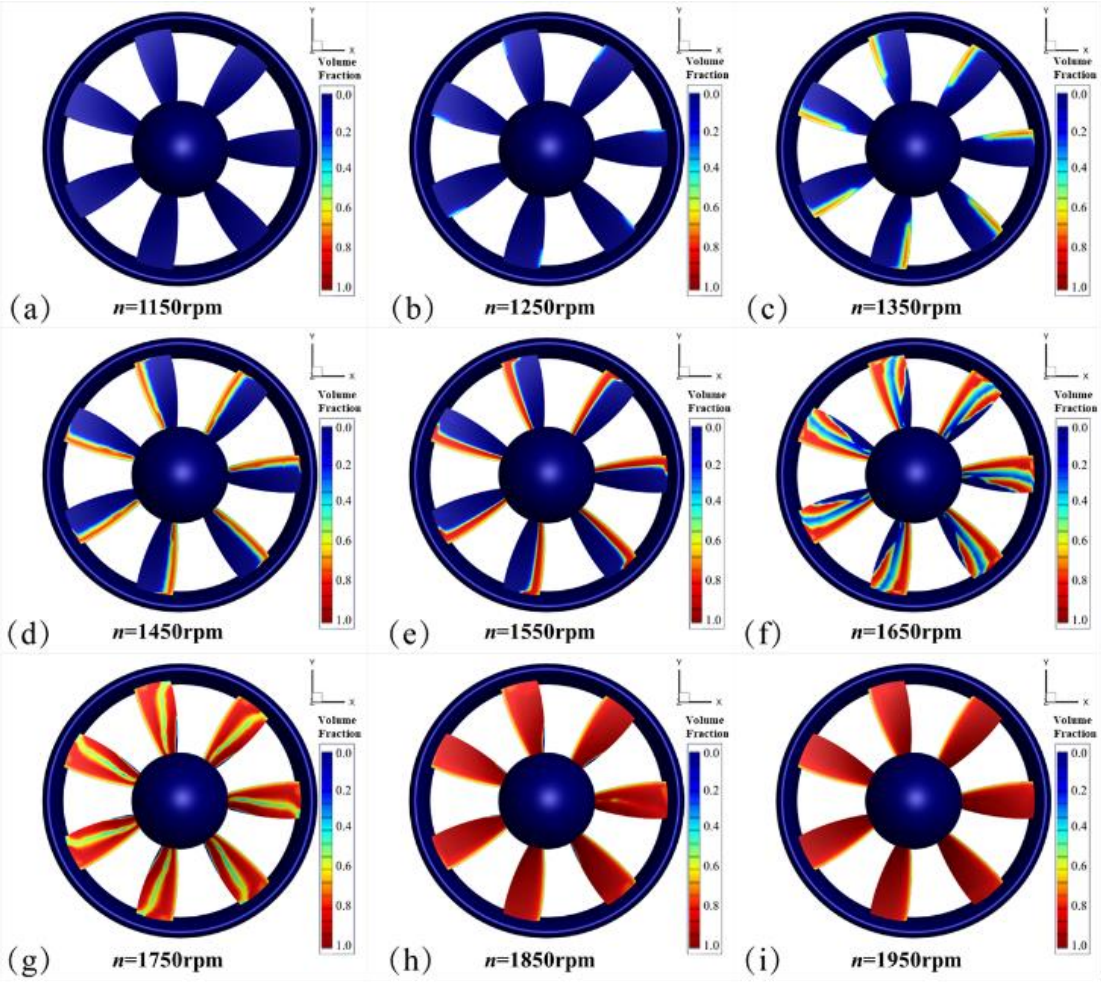

Fig. 11 Vapor volume fraction distribution on blades of the pump at different rotational speeds

hydrodynamic performance of the pump-jet propeller at a rotational speed of 1250 rpm under varying cavitation coefficients. As the cavitation coefficient decreases, there is a gradual decline in the thrust coefficient, torque coefficient, and efficiency of the pump-jet propeller. This trend demonstrates that cavitation significantly impairs the hydrodynamic performance of the pump-jet propeller, leading to reduced operational efficiency and diminished thrust output. Notably, the thrust coefficient and efficiency are more adversely affected by cavitation, whereas the torque coefficient exhibits a slower rate of decline.

5.2 Cavitation Flow around the Pump-jet Propeller

To analyze the cavitation performance of a pump-jet propeller at different rotational speeds, the evolution of cavitation was studied through the examination of the vapor volume fraction. Cavitation in the pump-jet propeller primarily occurs on the low-pressure suction side of the rotor and at the blade tip clearance. Figure 11 depicts the distribution of the vapor volume fraction on the rotor blade surface at a cavitation coefficient σ=2.73 and varying rotational speeds. The results indicate negligible cavitation at lower rotational speeds. However, as the rotational speed increases, a vortex region characterized by high-speed shear flow emerges within the pump-jet propeller, initiating cavitation. The cavitation area initially forms at the leading edge of the rotor blade tip and gradually expands toward the suction side. The presence of this cavitation zone causes the rotor to operate in a water vapor environment, leading to decreased thrust and torque, and consequently, a significant reduction in efficiency. This pattern correlates with the efficiency curve trends shown in Fig 9. At 1650 rpm, the cavitation zone encompasses nearly half of the blade area. When the speed further increases to 1750 rpm, cavitation extends over almost the entire blade surface, with the entire suction side and blade tip region completely enveloped by water vapor, which results in notable efficiency loss in the pump-jet propeller.

To analyze the flow field characteristics of the cavitating pump-jet propeller under three distinct operating conditions, speeds of 1150 rpm, 1250 rpm, and 1850 rpm were selected. These speeds correspond to the onset of cavitation, the point of optimal efficiency, and a higher operational speed, respectively. Figures 12, 13, and 14 depict the distributions of velocity fields on the axial plane at the inlet, outlet, and rotor-stator interface of the pump-jet propeller.

As depicted in the axial plane (a), the velocity distribution within the pump-jet propeller significantly diverges from that of the external flow field, due to the isolation created by the duct surrounding the propeller. With increasing rotational speeds, the flow velocity inside

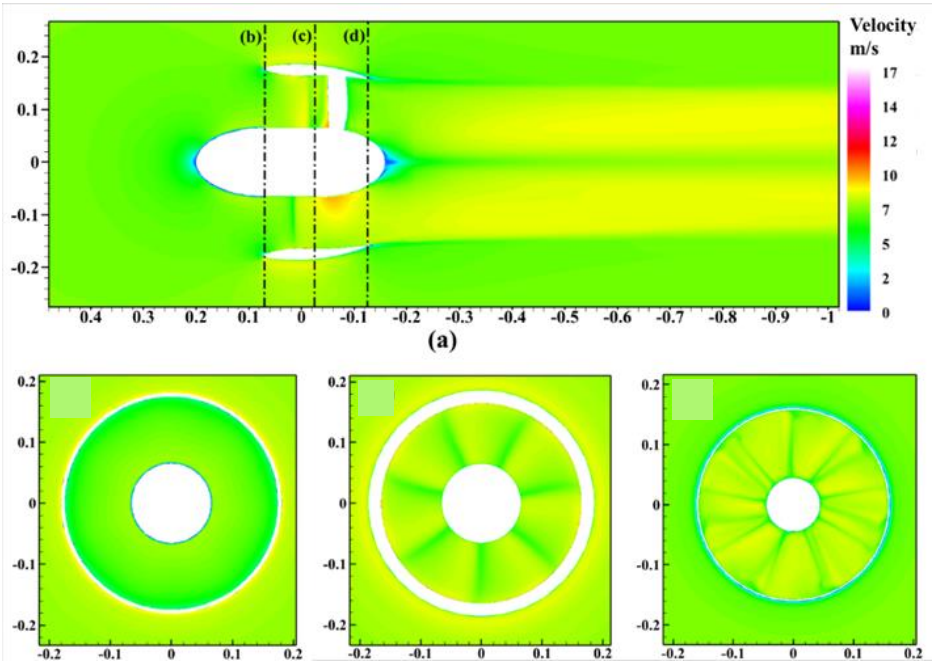

(b) (c) (d)

Fig. 12 Velocity distribution at a rotational speed of n=1150rpm: (a) the position of the axial plane section; (b) the inlet of pump-jet propeller; (c) the rotor-stator interface domain; (d) the outlet of pump-jet propeller

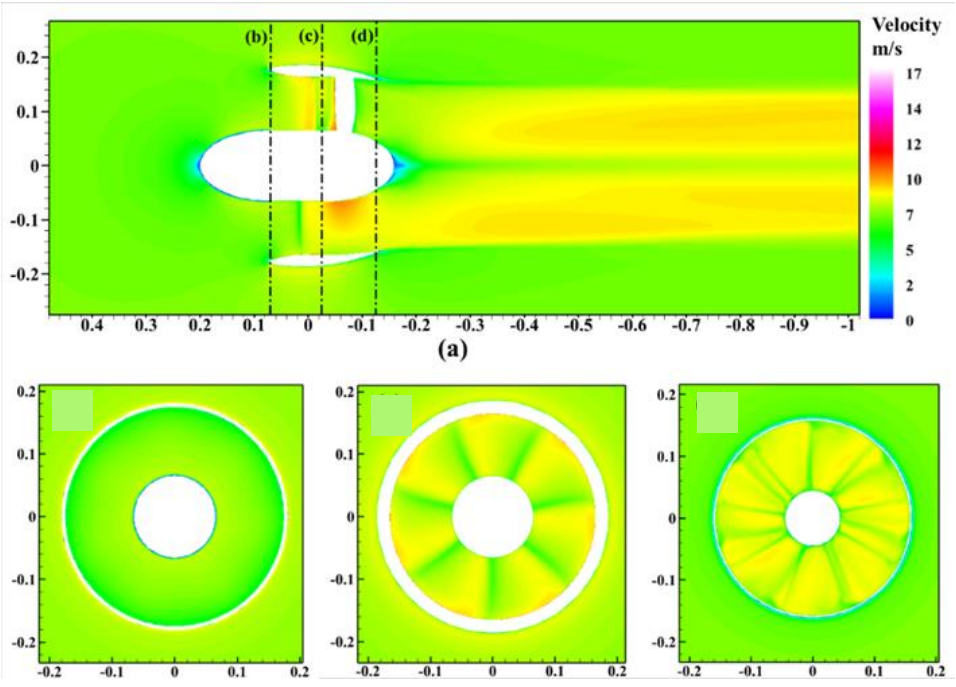

(b) (c) (d)

Fig. 13 Velocity distribution at a rotational speed of n=1250rpm: (a) the position of the axial plane section; (b) the inlet of pump-jet propeller; (c) the rotor-stator interface domain; (d) the outlet of pump-jet propeller

the pump-jet propeller escalates, particularly in the wake domain, where the duct's rectifying effect on the propeller is most pronounced. Figure (b) shows a relatively uniform circumferential distribution of inlet flow velocity, which is generally close to the ambient flow velocity. Nonetheless, variations are observed in the radial velocity distribution, with velocity decreasing progressively from the hub to the duct. This occurs because the inner half of the duct features a converging structure, while the hub section maintains a cylindrical form, leading to a more rapid increase in velocity at the hub as rotational speed rises. At the rotor-stator interface (c), the fluid velocity near the duct in the external flow field is notably higher than in the surrounding flow field. Within the internal flow field of the pump-jet propeller, the circumferential velocity distribution comprises 7 low-speed and 7 high-

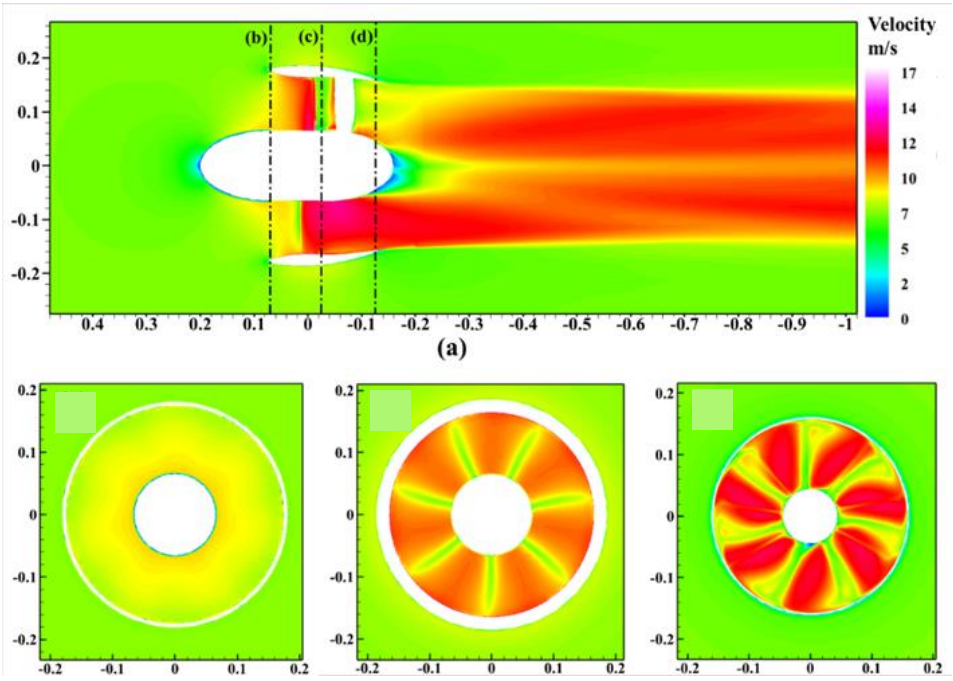

(b) (c) (d)

Fig. 14 Velocity distribution at a rotational speed of n=1850rpm: (a) the position of the axial plane section; (b) the inlet of pump-jet propeller; (c) the rotor-stator interface domain; (d) the outlet of pump-jet propeller

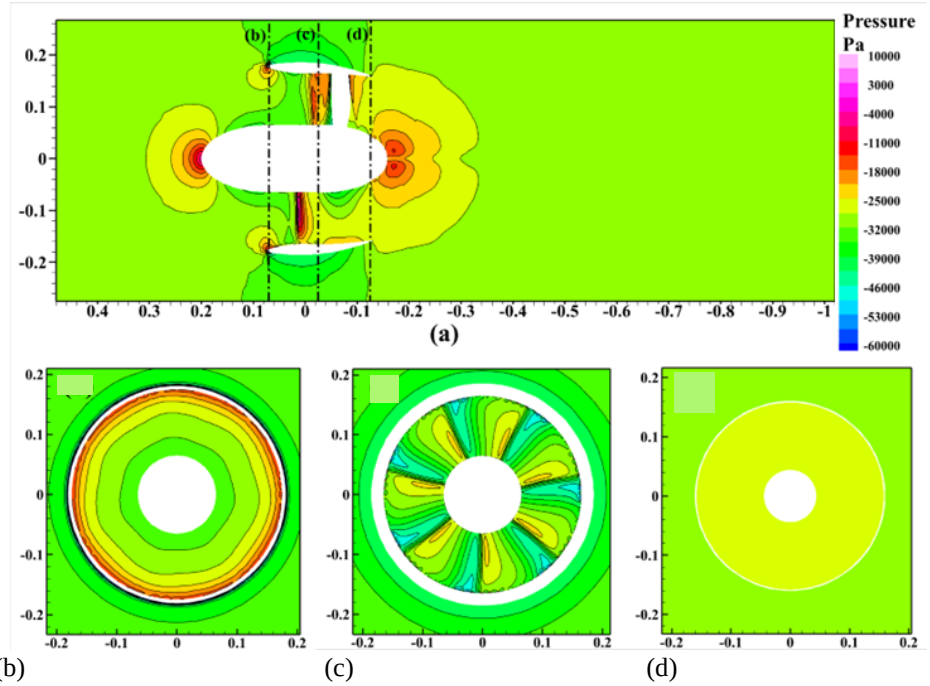

(b) (c) (d)

Fig. 15 Pressure distribution at a rotational speed of n=1150rpm: (a) the position of the axial plane section; (b) the inlet of pump-jet propeller; (c) the rotor-stator interface domain; (d) the outlet of pump-jet propeller

speed domains, corresponding to the rotor blades' number and arrangement. The disparity between the velocities in high-speed and low-speed domains intensifies with increasing rotational speed. At the pump-jet propeller outlet (d), following rectification by the stator, the flow is further segmented along the circumferential direction. The prevalence of high-speed domains predominantly reflects the rotor's influence, with diminishing impact from the stator as the rotational speed escalates.

Figures 15, 16, and 17 depict the pressure distribution at varying rotational speeds. From the axial view (a), it is evident that pressure within the pump-jet propeller changes significantly with rotational speed, with only minor variations in the pressure surrounding the external flow field. Higher pressures are observed near the backflow hood and the leading edge of the duct. At the pump-jet propeller outlet, the combination of high rotational fluid velocity and lower flow velocity at the tail

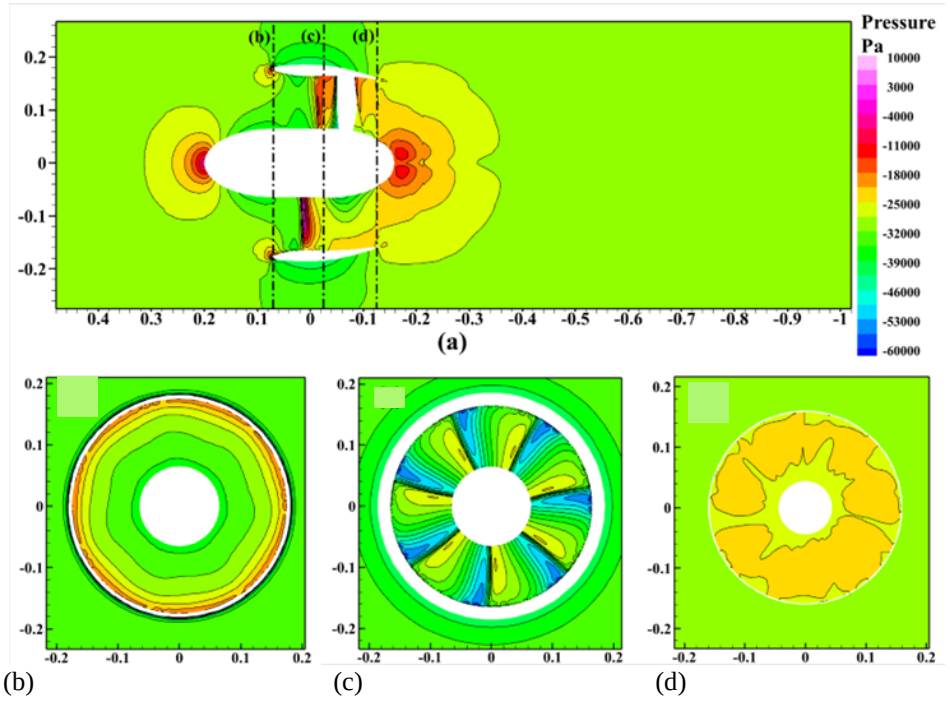

Fig. 16 Pressure distribution at a rotational speed of n=1250rpm: (a) the position of the axial plane section; (b)the inlet of pump-jet propeller; (c)the rotor-stator interface domain; (d)the outlet of pump-jet propeller

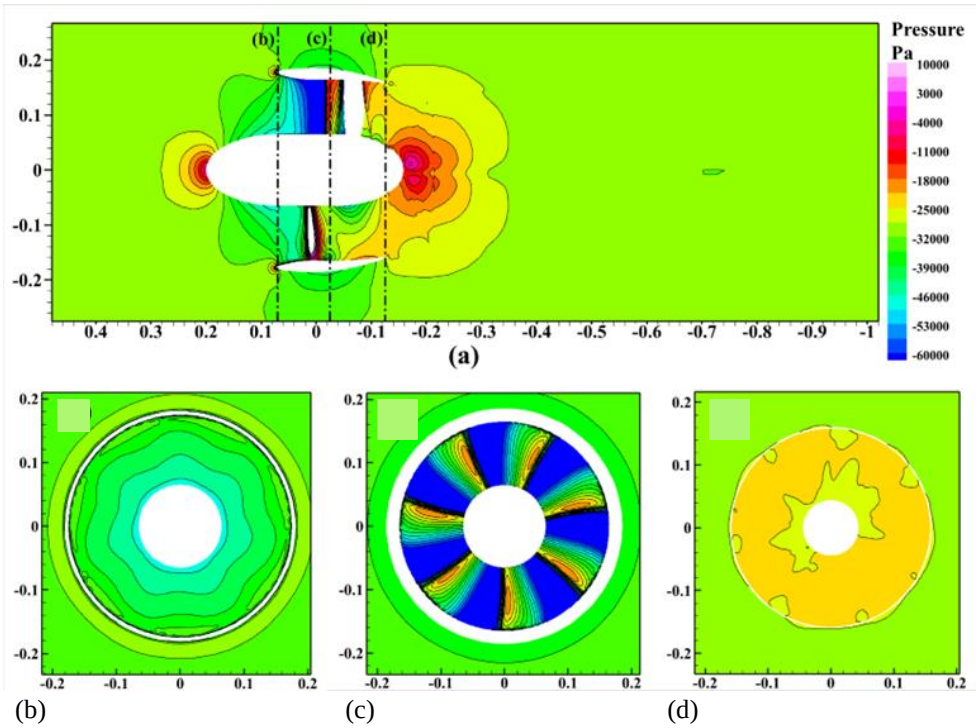

Fig. 17 Pressure distribution at a rotational speed of n=1850rpm: (a) the position of the axial plane section; (b) the inlet of pump-jet propeller; (c) the rotor-stator interface domain; (d) the outlet of pump-jet propeller

hood creates a circular high-pressure area centered around the rotational axis at the tail hood. At the pump-jet propeller inlet (b), pressure increases gradually from the hub to the duct, and the axial pressure distribution remains relatively uniform. As rotational speed increases, the suction capability at the inlet enhances, leading to a gradual reduction in the pressure gradient. Under low rotational speed conditions, the stagnation point at the duct moves closer to the inner side of the pump-jet propeller, influencing the surrounding flow field with high pressure and forming a ring-shaped high-pressure area. The interface between the moving and stationary parts (c) experiences high rotational instability of the rotor domain and a reverse velocity gradient from the stator, which contributes to an expansion in the low-pressure domain as rotational speed increases. At a rotational speed of 1850

rpm, the low-pressure area extends to cover nearly half of the area within the pump-jet propeller passage. Finally, the pressure distribution at the pump-jet propeller outlet (d) is relatively uniform and mirrors the pressure of the surrounding flow field.

In summary, the duct focuses the accelerated flow domain of the wake field, which contributes to a positive thrust effect and enhances the propulsion efficiency of the pump-jet propeller. As the rotational speed increases, the area of low pressure within the rotor domain expands, further indicating the intensification of cavitation at higher speeds.

5.3 Analysis of Calculation Results for Flow-induced Noise in the Fluid Acoustics Field

The hydrodynamic performance data were utilized as the foundation for calculating the cavitation noise of the pump-jet propeller, under an operating condition characterized by a cavitation number σ of 2.32 and a rotational speed n of 1250 rpm. A comparative analysis of the noise performance under this condition was conducted. To analyze the axial and radial sound pressure variations in the pump-jet propeller, 16 acoustic monitoring points were established in the noise simulation; eight were placed in the axial direction and eight in the radial direction. Figure 18 provides a schematic representation of the acoustic monitoring points' positions, where the blue area indicates the acoustic calculation domain grid. The initial monitoring point is situated 1D away from the center of the pump-jet propeller, with subsequent points positioned at every additional 1D interval. Axial monitoring points are labeled B_1 to B_8, and radial monitoring points are labeled B'_1 to B'_8.

Figure 19 illustrates the frequency spectrum associated with the sound pressure level in the pump-jet propeller operating under both non-cavitation and cavitation conditions. Notably, the blade passing frequency is prominently identified as the primary frequency in the noise fluctuations of the pump-jet propeller, characterized by periodic variations in amplitude. The maximum sound pressure typically occurs around this main frequency. Figures 19(a) and 19(b) display the sound pressure levels

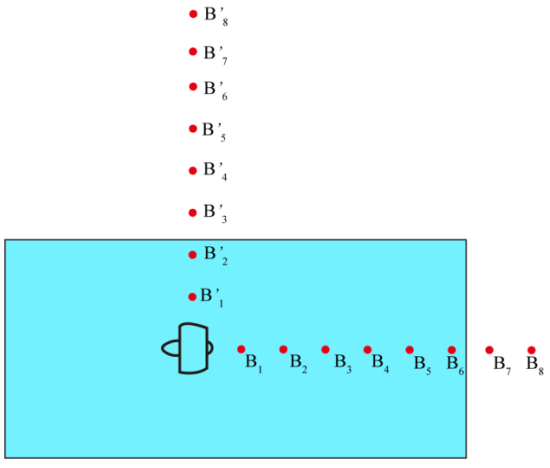

Fig. 18 Schematic diagram of monitoring points for pump spray noise sound field

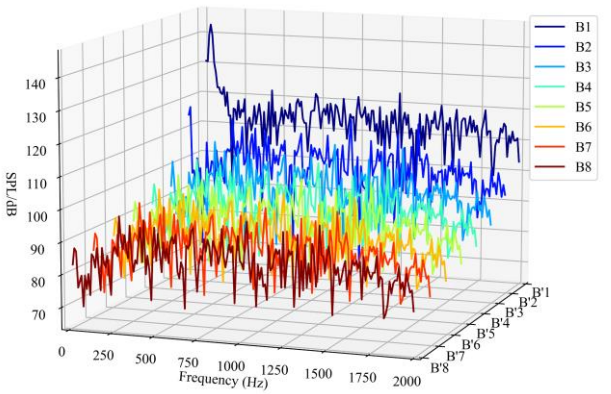

(a) Axial direction under non-cavitation conditions

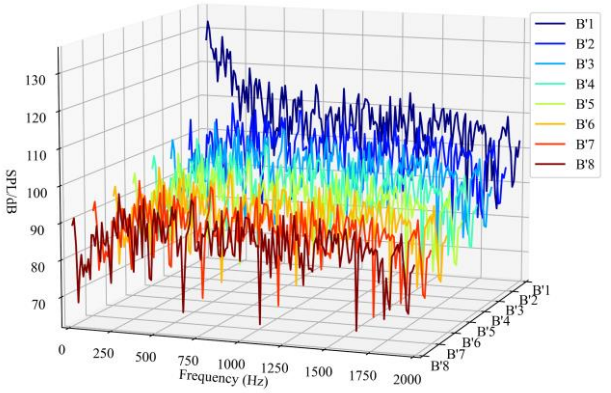

(b) Axial direction under non-cavitation condition

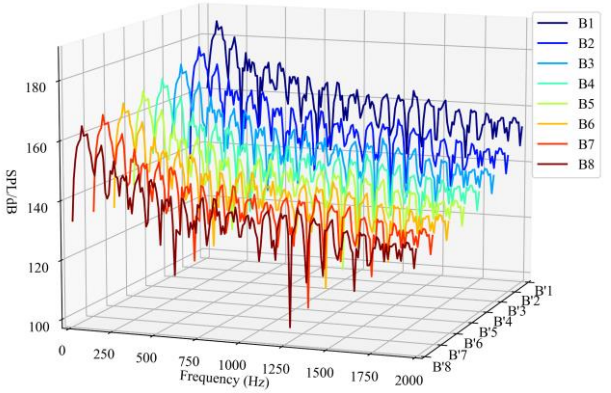

(c) Axial direction under cavitation conditions

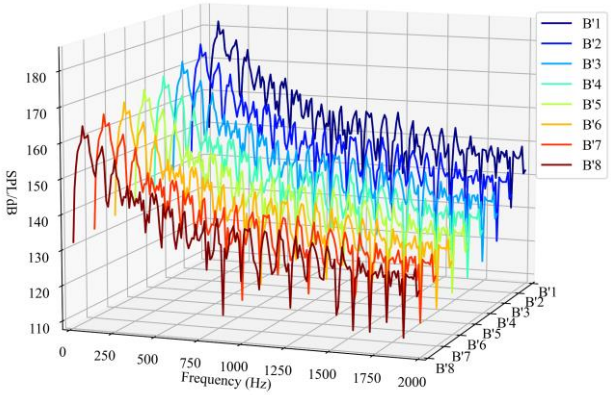

(d) Radial direction under cavitation conditions

Fig. 19 Sound pressure level spectrum distribution

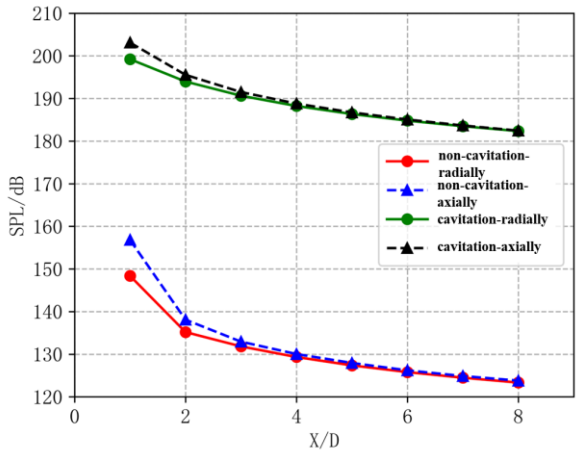

Fig. 20 Comparison of noise under cavitation and non-cavitation condition

at each monitoring point of the pump-jet propeller in the non-cavitating state. It is observed that the axial noise level exceeds the radial noise level, likely because the monitoring points are situated closer to the rotor area, thus being more affected by the rotor's movement. At the monitoring points nearest to the pump-jet propeller, such as at positions monitor B1 and monitor B'1, the low-frequency noise level is significantly elevated compared to other points, with sound pressure levels reaching above 130 dB. As the distance from the pump-jet propeller increases, the sound pressure levels at each monitoring point generally decline, with low-frequency sound pressure levels rapidly falling to around 90 dB.

Figures 19(c) and 19(d) illustrate the distribution of sound pressure curves at various monitoring points of the pump-jet propeller in the cavitating state. Both axial and radial sound pressures exhibit a decreasing trend with increasing frequency, with the maximum sound pressure levels observed in the low-frequency band. As monitoring points are positioned further from the center of the pump-jet propeller, the sound pressure values at equivalent frequencies show a declining trend. Moreover, as frequency increases, the sound pressure levels progressively decrease. Notably, at the blade passing frequency, the sound pressure level exceeds 180 dB but diminishes to approximately 120 dB to 130 dB at a blade frequency of 2000 Hz.

Furthermore, a comparison of the sound pressure level results between non-cavitating and cavitating flow fields reveals that the cavitating flow field consistently exhibits higher sound pressure levels across all frequency ranges than the non-cavitating flow field. Specifically, cavitation contributes to an approximate increase of 50 dB in flow field noise.

Figure 20 presents a comparison of the overall sound pressure levels at various monitoring points within the pump-jet propeller. The overall sound pressure level reflects the magnitude of sound across the entire frequency range at each monitoring point. The graph shows that the sound pressure gradually attenuates as the monitoring point moves away from the pump. Initially, the attenuation rate is significant but diminishes with increasing distance. At a position one diameter away from the pump-jet propeller, the difference in overall sound pressure levels between the axial and radial directions is within 5 dB. This difference lessens as the distance increases. When the distance extends to four diameters from the pump-jet propeller, the sound pressure levels at the axial and radial monitoring points nearly equalize. Comparisons between conditions with and without cavitation reveal that cavitation contributes to an increase in noise of approximately 50 dB at the same monitoring point.

Figure 21 illustrates the comparison of sound pressure distributions under non-cavitating and cavitating flows

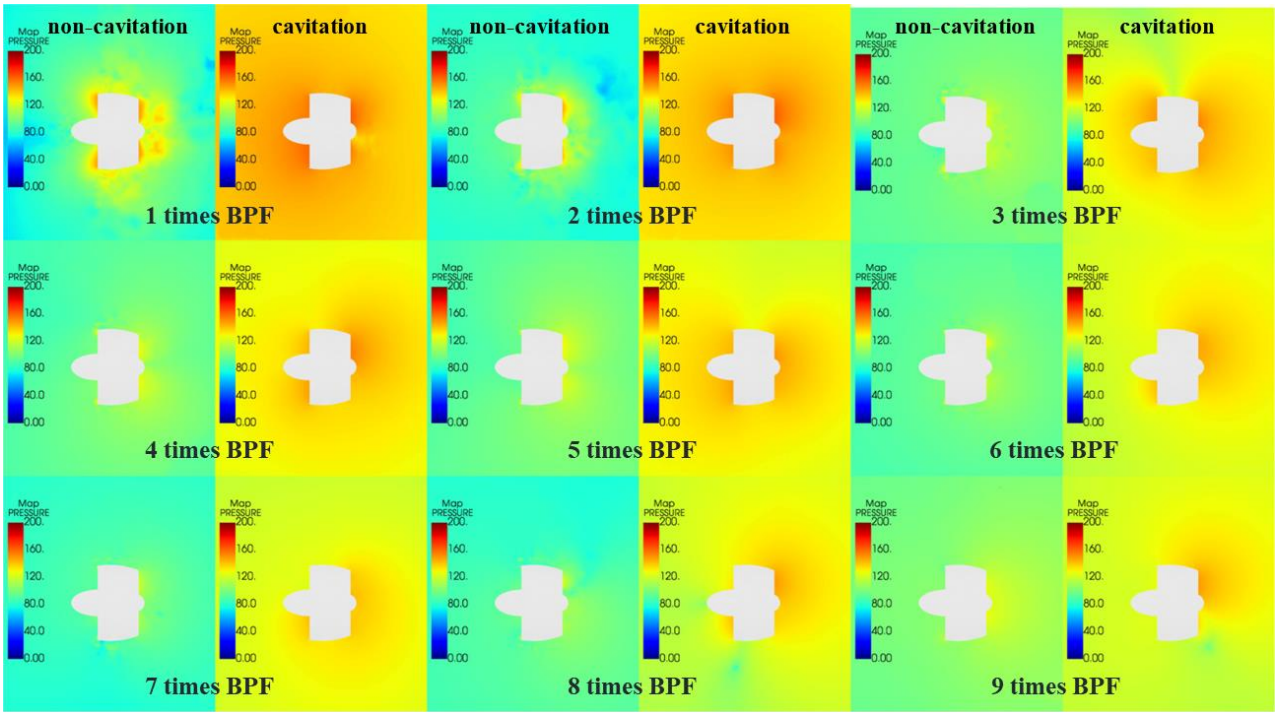

Fig. 21 Comparison of axial plane sound pressure under non-cavitating and cavitating conditions

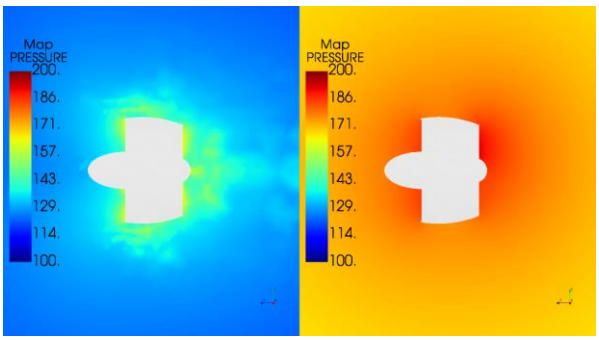

Fig. 22 Comparison of total sound pressure cloud maps between non-cavitating and cavitating conditions

across different frequency bands. In each frequency band, significantly higher sound pressure levels are observed under cavitation conditions than under non-cavitating conditions. Specifically, in the frequency band ranging from one to two times the blade passing frequency, higher sound pressure values are noted at the inlet and outlet of the guide vanes compared to the surrounding flow field, under both cavitating and non-cavitating conditions. In the frequency band ranging from three to eight times the blade passing frequency, the inlet sound pressure in the non-cavitating flow field approximates that of the surrounding flow field. In contrast, a markedly higher sound pressure distribution is observed at the inlet under cavitating conditions compared to the surrounding flow field. Moreover, sound pressure at the outlet of the pump-jet propeller decreases progressively with increasing frequency.

Figure 22 presents a comparison of the overall sound pressure distributions across different frequency bands in both non-cavitating and cavitating flows. The findings indicate that the total sound pressure range in the non-cavitating flow field spans from 100 dB to 150 dB, whereas in the cavitating flow field, it ranges from 150 dB to 200 dB. The overall sound pressure level in the cavitating flow field is significantly elevated compared to that in the non-cavitating flow field.

In summary, cavitating flow significantly exacerbates pump noise, independent of the volume pulsation noise associated with bubble dynamics. Monitoring data indicate that cavitation can lead to an increase in the overall sound pressure level by up to 50 dB. Therefore, suppressing cavitation is essential for enhancing the acoustic performance of the pump.

5.4 Sound Power Level Distribution

As previously discussed in the study, this section applies the sound power calculation method to analyze the sound power within the pump-jet propeller. Figure 23 depicts the cross-sectional distributions of sound power in the pump-jet propeller operating under varying cavitation coefficients. Analysis of the figure indicates that the sound power distribution in the pump-jet propeller's cavitation flow field predominantly concentrates along the inner wall of the conduit, within the space traversed by the impeller, and around the stator area. This results in a distinctive

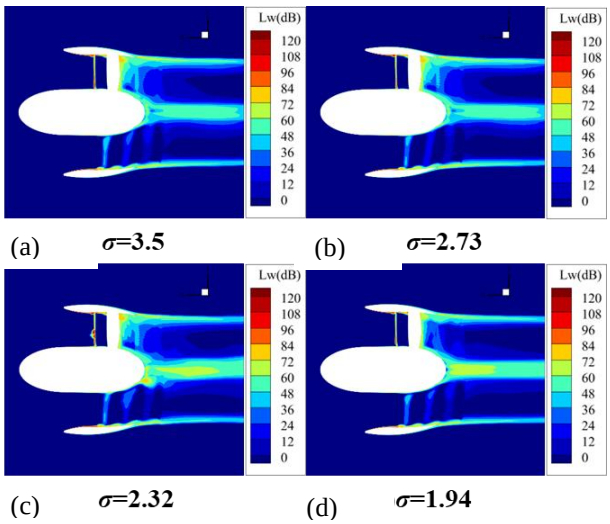

Fig 23 Sound power distribution in the cavitation flow field of pump-jet propeller at different cavitation numbers.

Fig. 23 illustrates the sound power distribution in the cavitation flow field of a pump-jet propeller at different cavitation numbers. Fig 24 depicts the sound power distribution in the axial section near the tip clearance. The analysis of the figure demonstrates that within the pump's cavitation flow field, the interaction between the liquid jet and surrounding gas initiates the formation of vortices and turbulence, which in turn facilitate the generation and propagation of sound energy. Particularly near the suction side of the pump impeller blades, the complexity of turbulence and vortex formation is heightened, thereby enhancing the divergence and spread of sound energy

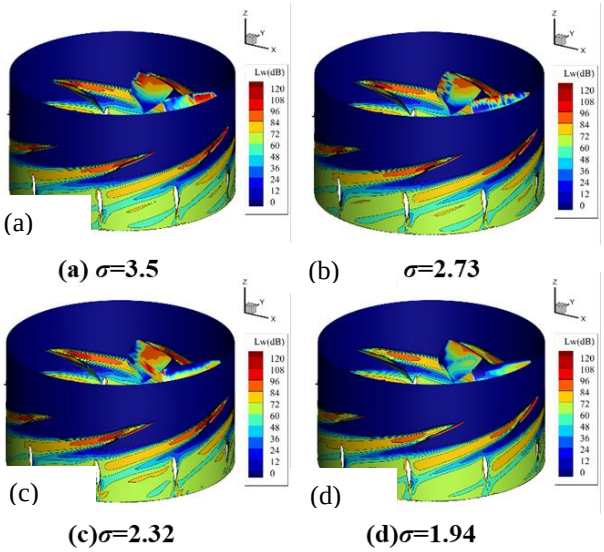

Fig. 24 Sound power distribution of axial section near the tip clearance

band-shaped sound field distribution in the wake field. Moreover, with decreasing cavitation numbers, a notable increase in sound power is observed in the wake field, ranging from approximately 55 dB to 70 dB.

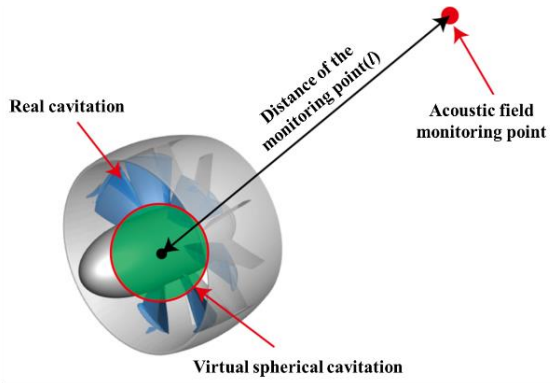

Fig. 25 Calculation Model for Volume Pulsation Radiated Noise of Cavitation

Consequently, regions with higher sound power distribution are predominantly located on the suction side of the pump impeller blades, with sound power levelsreaching approximately 100 dB. From the rotor domain to the stator domain, there is a gradual decrease in sound power. Within the stator domain, sound power values significantly decline and become relatively uniform, stabilizing at about 65 dB.

Under design conditions, the pump-jet propeller exhibits no severe cavitation, leading to no notable disparities in sound power distribution. Moreover, analysis of the sound power development trend reveals that the uniform distribution of higher sound power within the stator domain effectively mitigates noise across the entire domain.

5.5 Analysis of Radiated Noise from Bubble Volume Pulsation

Based on the analysis of internal void volume distribution presented in Section 5.2, it can be inferred that cavitation within the pump predominantly occurs at the suction side of the rotor blades. Consequently, the virtual void is established with its center at the rotor's rotation center. Additionally, the monitoring point is positioned 2 meters from the pump's rotor, as indicated by the red dot in Fig 25.

The volume pulsations of cavities within the pump-jet propeller were analyzed by collecting periodic numerical results from the last six full rotational cycles at varying cavitation coefficients. Figure 26 illustrates both time and frequency domain distributions of rotor bubble volumes under different cavitation coefficients. The red curve in the upper left corner of the figure displays the time-domain results of bubble volume changes over time, while the main graph depicts the frequency distribution obtained from the Fourier transform of bubble volume pulsations. These results are classified into three phases according to the cavitation development process: inception, development, and maturity of the cavitation bubbles.

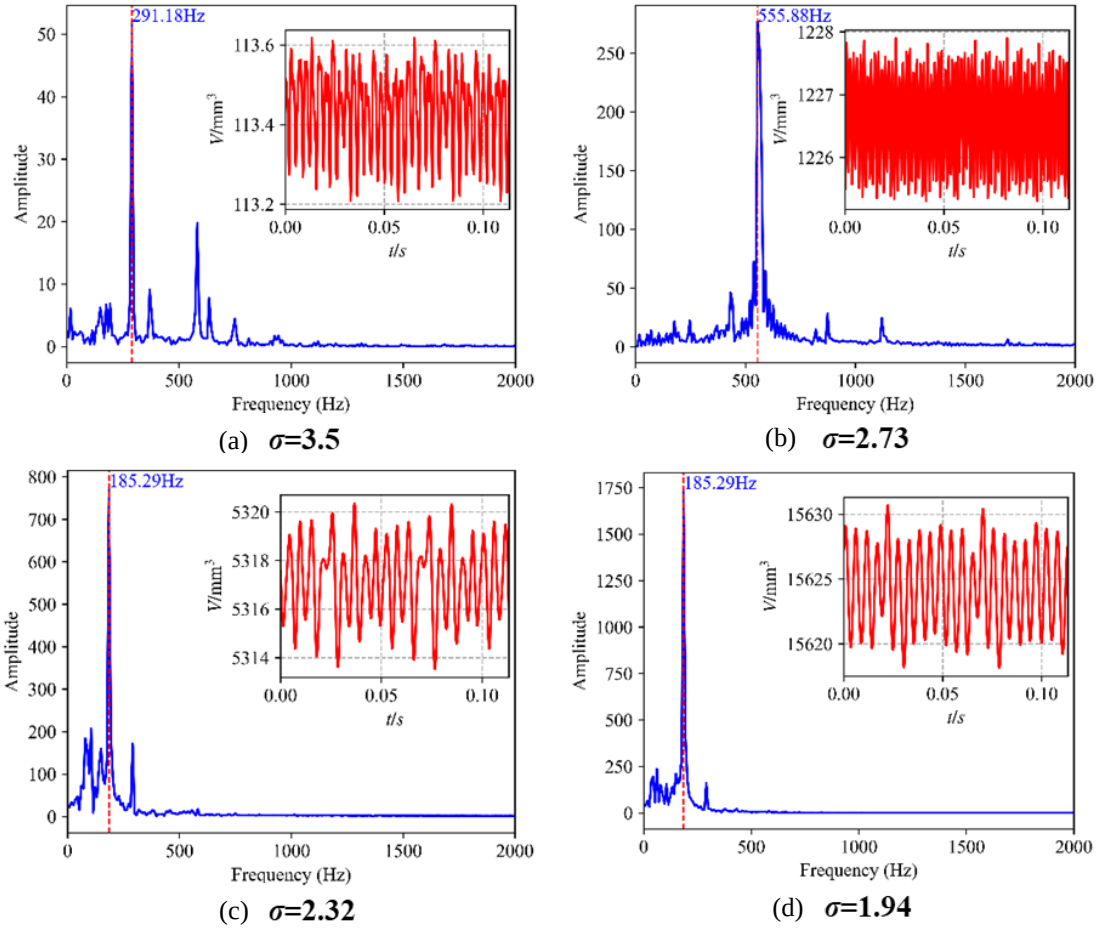

Fig. 26 Time and frequency domain results of bubble volume under different cavitation numbers

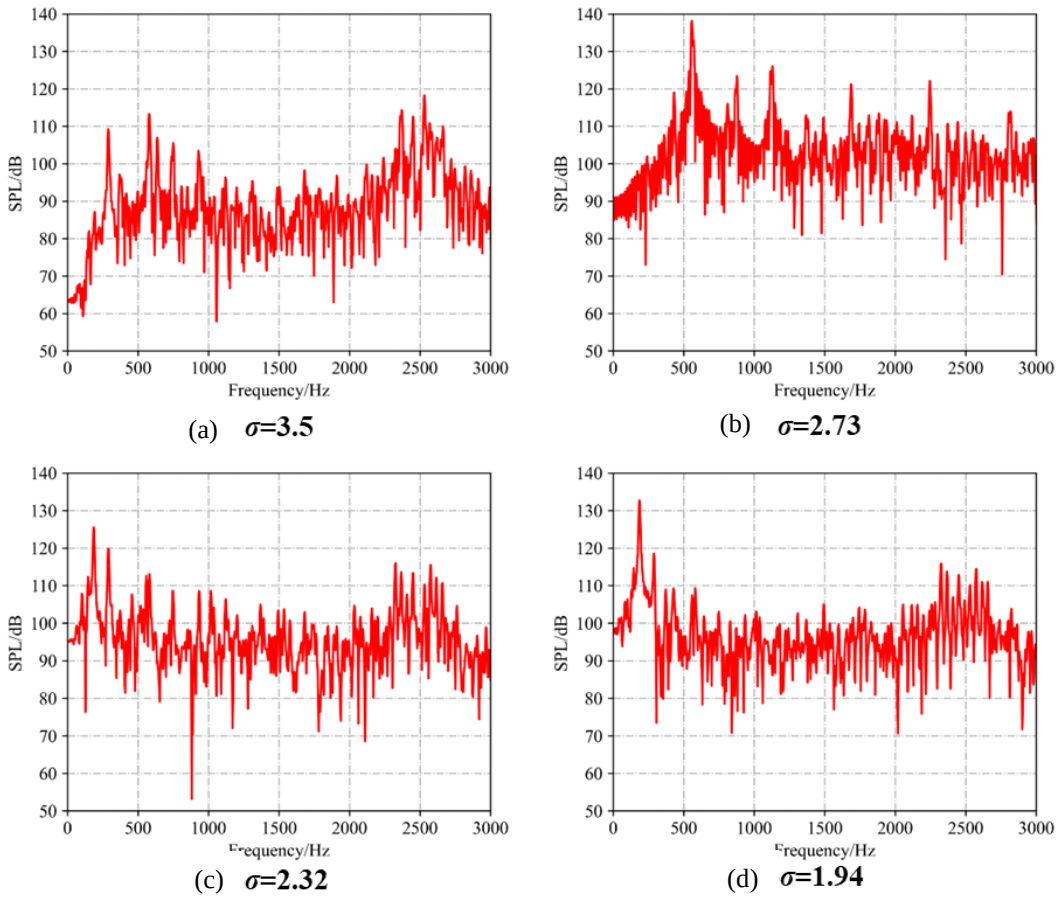

Fig. 27 Radiation noise spectrum of cavitation volume pulsation of pump-jet propeller under different cavitation numbers

In the inception stage of cavitation (σ=3.5), the volume of bubbles within the pump-jet propeller exhibits only periodic variations around a mean of 113 mm³ with minimal amplitude. From the frequency domain analysis of the Fourier transform, it is evident that the primary frequency of bubble volume pulsation is 291 Hz, with a fluctuation amplitude near 50. At this stage, the frequency of bubble shedding is twice that of the blade passing frequency, and a notable high amplitude is also observed at 555.88 Hz.

In the development stage of cavitation, with a cavitation coefficient σ equal to 2.73, the bubble volume periodically fluctuates around a mean value of 1227 mm³, exhibiting increases in both fluctuation amplitude and bubble size. Analysis of the frequency domain results shows that the fluctuation amplitude escalates, with the principal frequency of bubble volume pulsation identified at 555.88 Hz. At this stage, the frequency of bubble shedding is 3.8 times that of the blade passing frequency. This suggests that cavitation under these conditions is unstable, characterized by continuous high-frequency growth and collapse of bubbles, which may lead to the generation of high-frequency noise within the pump-jet propeller.

In the maturity stage of cavitation, when the cavitation coefficient σ reaches values of 2.32 and 1.94, cavitation becomes markedly more severe, and the volume of bubbles increases several-fold compared to earlier stages with higher cavitation coefficients. Despite the volume fluctuation values differing nearly threefold between these two cavitation numbers, the bubble shedding frequency remains approximately constant, close to one blade passing frequency. This suggests that following severe cavitation, the shape of the bubble gradually stabilizes, and the frequency of bubble volume pulsation is fundamentally associated with the blade passing frequency.

Overall, throughout the cavitation development process from the initial to the mature stage, the size and amplitude of volume pulsations in cavitation bubbles increase. The shedding frequency of these bubbles escalates from twice the blade passing frequency in the initial stage to 3.8 times at the developed stage, with a notable increase in fluctuation amplitude. This phase is characterized by high-frequency generation and collapse of bubbles. In the mature stage, the frequency of bubble shedding stabilizes, consistently maintaining at approximately one blade passing frequency.

Figure 27 displays the theoretical calculation results of cavitation bubble radiation noise, based on the spherical bubble radiation theory outlined earlier in this study. It includes frequency domain results under four distinct cavitation conditions. As depicted in this figure, the sound pressure amplitude initially increases to a peak value,

subsequently decreases, and stabilizes around a specific sound pressure level. Across various stages of cavitation development, the characteristic frequency of the cavitation bubble differs. The frequency corresponding to the maximum sound pressure amplitude aligns with the bubble shedding frequency shown in the figure. After severe cavitation, the highest sound pressure level of bubble noise occurs at one blade passing frequency. In the intermediate and low-frequency ranges, during the developing stage of bubbles, the volume pulsation radiation noise is relatively concentrated. The noise sound pressure follows distinct developmental patterns under varying cavitation coefficients. Under operating conditions with a cavitation coefficient σ of 1.94, the volume pulsation radiation sound pressure of cavitation bubbles exhibits more pronounced temporal variations, and the noise amplitude remains uniform in the high-frequency range.

6. CONCLUSION

This study primarily focused on the cavitation performance and noise characteristics of pump-jet propellers during underwater operation. The main findings are summarized as follows:

(1) The operational efficiency of the pump-jet impeller is directly impacted by increases in rotational speed and reductions in the cavitation coefficient, both of which intensify cavitation within the propeller. Cavitation significantly reduces hydrodynamic performance, occurring when the pressure on the suction side of the rotor blades falls below the saturation vapor pressure of the local environment due to increased rotational speeds.

(2) The overall sound pressure level of the pump-jet propeller ranges from 100 dB to 150 dB under non-cavitating conditions and from 150 dB to 200 dB under cavitating conditions. Cavitation greatly exacerbates flow-induced noise, with axial and radial sound pressure levels at identical positions approximately 50 dB higher than those in non-cavitating conditions.

(3) The volume pulsation size and amplitude of the bubbles in the pump-jet increase through the initial growth, development, and maturity stages. The characteristic frequencies of the bubbles vary at different cavitation stages. The shedding frequency of the bubbles correlates with the rotor blade passing frequency, and the frequency associated with the maximum sound pressure level matches the shedding frequency of the bubbles. The highest noise pressure level observed during cavitation development reaches up to 140 dB. The radiation noise from bubble volume pulsations primarily falls within the low and medium frequency bands.

This study has made exploratory efforts into understanding cavitation flow and its induced noise, yet some limitations persist. The cavitation model employed did not consider the impact of rotor rotation on the duct walls. Future research could enhance the cavitation model to enable a more comprehensive investigation of this effect. Additionally, given the significant noise produced by shock waves from bubble collapse, further studies could explore the noise specifically caused by this process. Although this study predominantly relied on numerical simulations of cavitation and its induced noise, integrating experimental data with these simulations could enrich the analysis in future research endeavors.

ACKNOWLEDGEMENTS

This research is supported by Institute of Fluid Engineering Equipment, Natural Science Foundation of Jiangsu Province (Grant No. BK20180879), High-level Talent Research Foundation of Jiangsu University (Grant No.18JDG012), National Key Research and Development Plan Project (Grant No. 2018YFB0606103) and Construction of Dominant Disciplines in Colleges and Universities and Universities in Jiangsu (PAPD).

CONFLICT OF INTEREST

The authors have no competing interests or conflicts to disclose.

AUTHORS CONTRIBUTION

Peiyi Zhang and **Jianping Yuan:** Conceptualization; methodology; formal analysis; writing original draft. **Yanxia Fu**，**Xueliang Hou**，**Jialin Hao:** writing review and editing. All authors have read and agreed to the published version of the manuscript.

REFERENCES

Al-Obaidi, A. (2018). *Experimental and numerical investigations on the cavitation phenomenon in a centrifugal pump* [Doctoral dissertation, University of Huddersfield]. *Huddersfield, UK*. Ahmed Al-Obaidi FINAL THESIS. PDF (hud.ac.uk)

Al-Obaidi, A. (2024). Effect of different guide vane configurations on flow field investigation and performances of an axial pump based on CFD analysis and vibration investigation. *Experimental Techniques*, *48*(1), 69-88. https://doi.org/10.1007/s40799-023-00641-5

Al-Obaidi, A. R. (2023). Experimental diagnostic of cavitation flow in the centrifugal pump under various impeller speeds based on acoustic analysis method. *Archives of Acoustics*, *48*(2), 159–170. https://doi.org/10.24425/aoa.2023.145234

Avanzi, F., Baù, A., De Vanna, F., & Benini, E. (2023). Numerical Assessment of a two-phase model for propulsive pump performance prediction. *Energies*, *16*(18), 6592. https://doi.org/10.3390/math9040343

Chang, H., Li, W., Shi, W., & Liu, J. (2018). Effect of blade profile with different thickness distribution on the pressure characteristics of novel self-priming pump. *Journal of the Brazilian Society of Mechanical Sciences and Engineering*, *40*, 1-20. https://doi.org/10.1007/s40430-018-1440-x

Furuya, O., & Chiang, W. L. (1988). *A new pumpjet design theory*. Honeywell Inc Hopkins Mn.

Gan, G., Duan, Y., Yi, J., Fu, Q., Zhu, R., & Shi, W. (2023a). Effect of tip clearance on the cavitation performance of high-speed pump-jet propeller. *Processes*, *11*(11), 3050. https://doi.org/10.3390/pr11113050

Gan, G., Shi, W., Yi, J., Fu, Q., Zhu, R., & Duan, Y. (2023b). The transient characteristics of the cavitation evolution of the shroud of high-speed pump-jet propellers under different operating conditions. *Water*, *15*(17), 3073. https://doi.org/10.3390/w15173073

Gangipamula, R., Ranjan, P., & Patil, R. S. (2023). Comparative studies on air borne noise and flow induced noise of a double suction centrifugal pump. *Applied Acoustics*, *202*, 109148. https://doi.org/10.1016/j.apacoust.2022.109148

Ghasemian, M., & Nejat, A. (2015). Aero-acoustics prediction of a vertical axis wind turbine using Large Eddy Simulation and acoustic analogy. *Energy*, *88*, 711-717. https://doi.org/10.1016/j.energy.2015.05.098

Han, C. Z., Xu, S., Cheng, H. Y., Ji, B., & Zhang, Z. Y. (2020). LES method of the tip clearance vortex cavitation in a propelling pump with special emphasis on the cavitation-vortex interaction. *Journal of Hydrodynamics*, *32*(6), 1212-1216. https://doi.org/10.1007/s42241-020-0070-9

Han, R., Yu, H., Hua, H., Li, H., Huang, X., & Dong, X. (2023). Experimental study of controlling clearance flow in a pump-jet propulsor. *Chinese Journal of Ship Research*, *18*(1). https://doi.org/10.19693/j.issn.1673-3185.02419

Hashem, I., Mohamed, M. H., & Hafiz, A. A. (2017). Aero-acoustics noise assessment for Wind-Lens turbine. *Energy*, *118*, 345-368. https://doi.org/10.1016/j.energy.2016.12.049

Huang, X., Shi, S., Su, Z., Tang, W., & Hua, H. (2022). Reducing underwater radiated noise of a SUBOFF model propelled by a pump-jet without tip clearance: Numerical simulation. *Ocean Engineering*, *243*, 110277. https://doi.org/10.1016/j.oceaneng.2021.110277

Ji, X., Dong, X., & Yang, C. (2021). Attenuation of the tip-clearance flow in a pump-jet propulsor by thickening and raking the tips of rotor blades: A numerical study. *Applied Ocean Research*, *113*, 102723. https://doi.org/10.1016/j.apor.2021.102723

Kowalczyk, S., & Felicjancik, J. (2016). Numerical and experimental propeller noise investigations. *Ocean Engineering*, *120*, 108-115. https://doi.org/10.1016/j.oceaneng.2016.01.032

Li, F., Huang, Q., Pan, G., Wu, B., & Li, H. (2023a). Transient analysis of the pre-whirl pump-jet propulsor with different blade numbers. *Ships and Offshore Structures*, *18*(6), 846-858. https://doi.org/10.1080/17445302.2022.2076992

Li, H., Huang, Q., & Pan, G. (2023b). Numerical radiated noise prediction of a pre-swirl stator pump-jet propulsor. *Journal of Marine Science and Application*, *22*(2), 344-358. https://doi.org/10.1007/s11804-023-00340-y

Li, H., Huang, Q., Pan, G., Dong, X., & Li, F. (2022). An investigation on the flow and vortical structure of a pre-swirl stator pump-jet propulsor in drift. *Ocean Engineering*, *250*, 111061. https://doi.org/10.1016/j.oceaneng.2022.111061

Lighthill, M. J. (1952). On sound generated aerodynamically I. General theory. *Proceedings of the Royal Society of London. Series A. Mathematical and Physical Sciences*, *211*(1107), 564-587. https://doi.org/10.1098/rspa.1952.0060

Menter, F. R. (1994). Two-equation eddy-viscosity turbulence models for engineering applications. *AIAA Journal*, *32*(8), 1598-1605. https://doi.org/10.2514/3.12149

Mohamed, M. (2016). Reduction of the generated aero-acoustics noise of a vertical axis wind turbine using CFD (Computational Fluid Dynamics) techniques. *Energy*, *96*, 531-544. https://doi.org/10.1016/j.energy.2015.12.100

Proudman, I. (1952). The generation of noise by isotropic turbulence. *Proceedings of the Royal Society of London. Series A. Mathematical and Physical Sciences*, *214*(1116), 119-132. https://doi.org/10.1098/rspa.1952.0154

Qin, D., Pan, G., Lee, S., Huang, Q., & Shi, Y. (2019). Underwater radiated noise reduction technology using sawtooth duct for pumpjet propulsor. *Ocean Engineering*, *188*, 106228. https://doi.org/10.1016/j.oceaneng.2019.106228

Qiu, C., Huang, Q., Pan, G., Shi, Y., & Dong, X. (2020). Numerical simulation of hydrodynamic and cavitation performance of pumpjet propulsor with different tip clearances in oblique flow. *Ocean Engineering*, *209*, 107285. https://doi.org/10.1016/j.oceaneng.2020.107285

Satyanarayana, B., Ramji, K., & Rao, M. N. (2010). Cavitation studies on axi-symmetric underwater body with pumpjet propulsor in cavitation tunnel. *International Journal of Naval Architecture and Ocean Engineering*, *2*(4), 185-194. https://doi.org/10.2478/IJNAOE-2013-0035

Shi, S., Huang, X., Rao, Z., Su, Z., & Hua, H. (2022). Numerical analysis on flow noise and structure-borne noise of fully appended SUBOFF propelled by a pump-jet. *Engineering Analysis with Boundary Elements*, *138*, 140-158. https://doi.org/10.1016/j.enganabound.2022.02.012

Si, Q., Ali, A., Liao, M., Yuan, J., Gu, Y., Yuan, S., & Bois, G. (2023). Assessment of cavitation noise in a centrifugal pump using acoustic finite element

method and spherical cavity radiation theory. *Engineering Applications of Computational Fluid Mechanics*, *17*(1), 2173302. https://doi.org/10.1080/19942060.2023.2173302

Si, Q., Shen, C., He, X., Li, H., Huang, K., & Yuan, J. (2020). Numerical and experimental study on the flow-induced noise characteristics of high-speed centrifugal pumps. *Applied Sciences*, *10*(9), 3105. https://doi.org/10.3390/app10093105

Spalart, P. R. (1997). *Comments on the Feasibility of LES for Wings and on the Hybrid RANS/LES Approach.* [Conference session]. Proceedings of the First AFOSR International Conference on DNS/LES.

Su, Z., Shi, S., Huang, X., Rao, Z., & Hua, H. (2021). Vibro-acoustic characteristics of a coupled pump-jet–shafting system–SUBOFF model under distributed unsteady hydrodynamics by a pump-jet. *Ocean Engineering*, *235*, 109429. https://doi.org/10.1016/j.oceaneng.2021.109429

Sun, Y., Peng, H., Liu, W., Guo, J., & Guo, Y. (2022). Comparison of the hydrodynamic performance of front and rear-stator pump-jet propulsors in an oblique wake under the cavitation condition. *Physics of Fluids*, *34*(3). https://doi.org/10.1063/5.0082769

Vaz, G., Hally, D., Huuva, T., Bulten, N., Muller, P., Becchi, P., Herrer, J., Whitworth, S., Macé, R., & Korsström, A. (2015, May). Cavitating flow calculations for the E779A propeller in open water and behind conditions: code comparison and solution validation [Conference session]. Proceedings of the 4th International Symposium on Marine Propulsors, Austin, TX, USA (Vol. 31). https://www.researchgate.net/publication/275622126_Cavitating_Flow_Calculations_for_the_E779A_Propeller_in_Open_Water_and_Behind_Conditions_Code_Comparison_and_Solution_Validation

Xu, Z., & Lai, H. (2023). Comparison of cavitation in two axial-flow water jet propulsion pumps. *Processes*, *11*(7), 2137. https://doi.org/10.3390/pr11072137

Yuan, J., Chen, Y., Wang, L., Fu, Y., Zhou, Y., Xu, J., & Lu, R. (2020). Dynamic analysis of cavitation tip vortex of pump-jet propeller based on DES. *Applied Sciences*, *10*(17), 5998. https://doi.org/10.3390/app10175998

Zhang, Y., Han, J., Ji, S., Wu, R., Huang, B., Zhang, D., & Wu, D. (2024). Excitation force on a pump-jet propeller: The clocking effect of pre-swirl stator. *Ocean Engineering*, *293*, 116711. https://doi.org/10.1016/j.oceaneng.2024.116711

Zhao, X., Shen, X., Geng, L., Zhang, D., & van Esch, B. B. (2022). Effects of cavitation on the hydrodynamic loading and wake vortex evolution of a pre-swirl pump-jet propulsor. *Ocean Engineering*, *266*, 113069.. https://doi.org/10.1016/j.oceaneng.2022.113069

Zhou, Y., Pavesi, G., Yuan, J., & Fu, Y. (2022). A review on hydrodynamic performance and design of pump-jet: Advances, challenges and prospects. *Journal of Marine Science and Engineering*, *10*(10), 1514. https://doi.org/10.3390/jmse10101514

Zwart, P. J., Gerber, A. G., & Belamri, T. (2004). *A two-phase flow model for predicting cavitation dynamics* [Conference session]. Fifth International Conference on Multiphase Flow, Yokohama, Japan. https://www.researchgate.net/publication/306205415